Available on CMS information server

CMS NOTE -2018/002

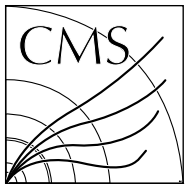

The Compact Muon Solenoid Experiment

CMS Note

Mailing address: CMS CERN, CH-1211 GENEVA 23, Switzerland

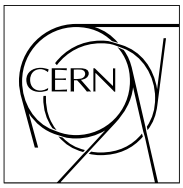

08 February 2018 (v3, 03 May 2018)

Front-side biasing of n-in-p silicon strip detectors

Marta Baselga, Thomas Bergauer, Alexander Dierlamm, Marko Dragicevic, Axel König, Elias Pree, Marius Metzler

Abstract

Front-side biasing is an alternative method to bias a silicon sensor. Instead of directly applying high voltage to the back-side, one can exploit the conductive properties of the edge region to bias a detector exclusively via top-side connections. This option can be beneficial for the detector design and might help to facilitate the assembly process of modules. The effective bias voltage is affected by the resistance of the edge region and the sensor current. The measurements of n-in-p sensors performed to qualify this concept have shown that the voltage drop emerging from this resistance is negligible before irradiation. After irradiation, however, the resistivity of the edge region increases with fluence and saturates in the region of $10^7\ \Omega$ at a fluence of $1 \cdot 10^{15}\ \mathrm{n_{eq}cm^{-2}}$. The measurements are complemented by TCAD simulations and interpretations of the observed effects.

Front-side biasing of n-in-p silicon strip detectors

Marta Baselga[a], Thomas Bergauer[b], Alexander Dierlamm[a], Marko Dragicevic[b], Axel König[b], Marius Metzler[a,*], Elias Pree[b]

[a] *ETP (KIT), Hermann-von-Helmholtz-Platz 1, 76344 Eggenstein-Leopoldshafen, Germany*
[b] *HEPHY, Nikolsdorfer Gasse 18, 1050 Wien, Austria*

Abstract

Front-side biasing is an alternative method to bias a silicon sensor. Instead of directly applying high voltage to the back-side, one can exploit the conductive properties of the edge region to bias a detector exclusively via top-side connections. This option can be beneficial for the detector design and might help to facilitate the assembly process of modules. The effective bias voltage is affected by the resistance of the edge region and the sensor current. The measurements of n-in-p sensors performed to qualify this concept have shown that the voltage drop emerging from this resistance is negligible before irradiation. After irradiation, however, the resistivity of the edge region increases with fluence and saturates in the region of $10^7\,\Omega$ at a fluence of $1 \cdot 10^{15}\,\mathrm{n_{eq}cm^{-2}}$. The measurements are complemented by TCAD simulations and interpretations of the observed effects.

Keywords: Silicon sensors, radiation hardness, front-side biasing

1. Introduction

Large silicon tracking devices, as they are used in modern high energy physics (HEP) experiments such as CMS, ATLAS or LHCb at the Large Hadron Collider (LHC), are composed of thousands of stand-alone units. These units are called modules and consist of one or multiple silicon sensors, front-end electronics, as well as support structures.

The conventional biasing scheme of a silicon strip sensor uses a ground connection on the top-side. The strip and bias implants, as well as their contact pads, are located there. A high voltage (HV) connection is applied to the back-side, which is usually covered by an aluminum layer. The top-side is easily accessible at nearly every step of the module assembly. The wire-bonding of the sensor channels as well as the attachment of the ground connection is therefore performed at the end of the module assembly process. Depending on the module

*Corresponding author
Email address: marius.metzler@kit.edu (Marius Metzler)

Table 1: List of sensors used in this study. The sensor nomenclature indicates the sensor design (first character) and the active sensor thickness in microns (digits). The D sensors were produced by IFX and are made of thinned float-zone material. All other samples were produced by HPK and are made of deep-diffused material with a physical thickness of 320 µm.

Sensor name	A_{sensor} (cm^2)	A_{edge} (cm^2)
A200	1.83	0.38
A240	1.83	0.38
B200	3.10	0.46
B240	3.10	0.46
C240	6.96	0.81
X240	96.66	2.54
D200	13.49	1.01

design, the back-side may become inaccessible by then, as it might be covered by another sensor or support structures. The HV connection must therefore be attached to the back-side, glued, wire-bonded, and encapsulated at the very beginning of the process. Building a reliable connection is a complicated task, which is not easy to achieve. Moreover, placing a sensor face down on the bonding support to be able to process the back-side can be a risky operation. However, it is in principle possible to exploit the conductive characteristics of the sensor edge in order to bias the sensor by two top-side connections. As a result, the sensor edge acts as a low-ohmic resistor, which interconnects the top-side edge contact and the back-side. This approach would eliminate time-consuming assembly steps and facilitate the module construction.

This study was performed in the framework of the CMS Phase-2 Tracker Upgrade, but the application of front-side biasing (FSB) is not confined to this particular application. The study investigates the validity of front-side biasing for modern HEP experiments in general. Characteristic measurements on small strip sensors (referred to as mini sensors in this paper) are compared under front-side-biased and back-side-biased modes of operation (back-side biasing: BSB). Furthermore, the edge resistivity and its dependence on temperature, fluence, and bias voltage is studied by evaluating experimental, theoretical, and simulated data. Eventually, the measured resistivities can be used to approximate the voltage drop and additional power consumption of a large front-side-biased silicon sensor before and after irradiation.

2. Experimental Setup and Simulation Environment

Table 1 lists the samples that were used in this study, and their edge areas and full surface areas, A_{edge} and A_{sensor}. The definition of A_{edge}, as well as a detailed description of sensor specific terms and design details, can be found

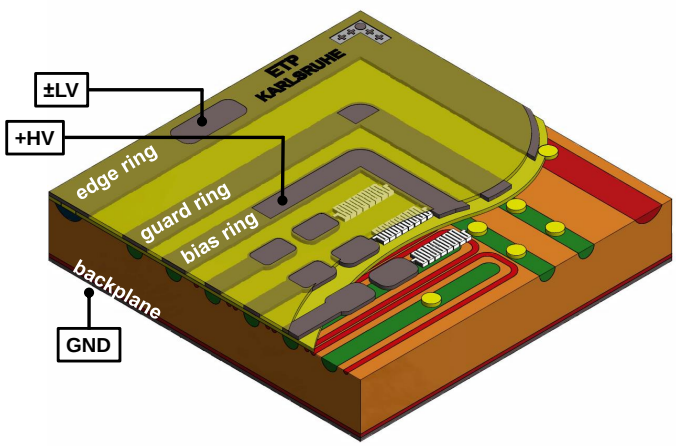

Figure 1: 3D sketch of the corner region of a standard strip sensor, which incorporates the scheme of an edge resistivity measurement. Voltage ramps are performed between edge ring and backplane to obtain the resulting current through the edge region. The backplane is grounded to create a common reference point (GND). The bias ring is set to a positive high voltage (HV). The edge ring can be set to either positive or negative low voltage potential (LV).

in Chapter 3. The corresponding detector wafers were fabricated by two different vendors. The sensors were produced with similar masks and designs, using different silicon materials. The wafers manufactured by HPK [1] are composed of deep-diffused[1] float-zone (ddFZ) silicon with a physical thickness of 320 µm. These samples have an active thickness of either 240 µm or 200 µm. The wafers processed by IFX [2] are made of float-zone silicon (FZ) that is physically thinned to 200 µm. The bulk material of all samples is p-doped silicon while the strip and bias ring implants are n-doped [3], referred to as n-in-p. The edge implant on the top-side as well as the backplane implant are p-doped. The doping concentration of the p-bulk is approximately $10^{12}\,\mathrm{cm}^{-3}$, while the value for strip, backside and edge implants is about $10^{19}\,\mathrm{cm}^{-3}$.

The edge resistivity measurements were performed in custom-made probe station setups at ETP (KIT) [4, 5] and HEPHY [6]. These setups provide temperature control and allow a sensor biasing up to full depletion or higher. To achieve bulk depletion while measuring the edge resistance at the same time, one has to utilize the measurement scheme presented in Figure 1 using two source measurement units (SMUs). The backplane is set to ground potential and acts as a common reference point for both units. In order to deplete an n-in-p sensor, the

[1]Deep-diffusion reduces the active thickness of the material by diffusing dopants from a highly doped backside implant further into the wafer bulk. This technology is intellectual property of HPK.

Table 2: Parameters of the irradiation model [9] used for TCAD simulations, using one donor and acceptor defect. The energy is given with respect to the valence band energy E_V and the conduction band energy E_C. The concentration is assumed to be proportional to the fluence Φ. The parameters σ(e) and σ(h) denote the electron and hole cross section of those defects.

Parameter	Donor	Acceptor
Energy (eV)	$E_V + 0.48$	$E_C - 0.525$
Conc. (cm^{-3})	$5.598\ cm^{-1} \times \Phi - 3.949 \cdot 10^{14}$	$1.189\ cm^{-1} \times \Phi + 6.454 \cdot 10^{13}$
σ(e) (cm^2)	$1.0 \cdot 10^{-14}$	$1.0 \cdot 10^{-14}$
σ(h) (cm^2)	$1.0 \cdot 10^{-14}$	$1.0 \cdot 10^{-14}$

n-doped implants need to be set to a higher potential than the p-doped bulk. The first SMU is therefore used to apply a positive high voltage to the bias ring and to measure the sensor's leakage current. An additional low voltage (LV) offset between backplane and edge region is realized by a second SMU, which measures the edge current.

Simulations were carried out with the Synopsys Sentaurus TCAD [7] toolkit, a simulation package for semiconductors using the finite element method. Different geometries and parameters were used for the simulations, in order to confirm the experimental results. Simulations were carried out with a simplified geometry of D200 and B240 (Table 1), which includes an extra wide bias ring instead of a bias ring and strips. This has proven to be a valid approximation, since the edge region is the major focus here and the results only differed by a negligible amount ($< 1\,\%$ difference for simulated edge currents of simplified and full geometry). The interface charge density between the silicon bulk and the silicon dioxide layer, N_{ox}, which is present in the edge region, is $10^{11}\,cm^{-2}$ for HPK sensors. According to Ref. [8], N_{ox} is about $2 \cdot 10^{10}\,cm^{-2}$ for unirradiated IFX sensors, which is incorporated into the simulations. The radiation model which was used is presented in Ref. [9]. The corresponding defect parameters of the simulations are listed in Table 2. The model is valid for fluences between $1 \cdot 10^{14}\,n_{eq}cm^{-2}$ and $1 \cdot 10^{15}\,n_{eq}cm^{-2}$. It postulates a constant number of positive interface oxide charges $N_{ox} = 1 \cdot 10^{12}\,cm^{-2}$ for proton irradiation.

Irradiations for this study were carried out with 23 MeV protons at ZAG [10]. Fluences ranged from $1 \cdot 10^{13}\,n_{eq}cm^{-2}$ up to $2 \cdot 10^{15}\,n_{eq}cm^{-2}$. The fluences for strip tracking detectors at the HL-LHC are expected to range from $3 \cdot 10^{14}\,n_{eq}cm^{-2}$ to $1 \cdot 10^{15}\,n_{eq}cm^{-2}$ for $3000\,fb^{-1}$ [11]. This depends on the geometry of the tracking device, the distance from the vertex and the position of a particular module layer.

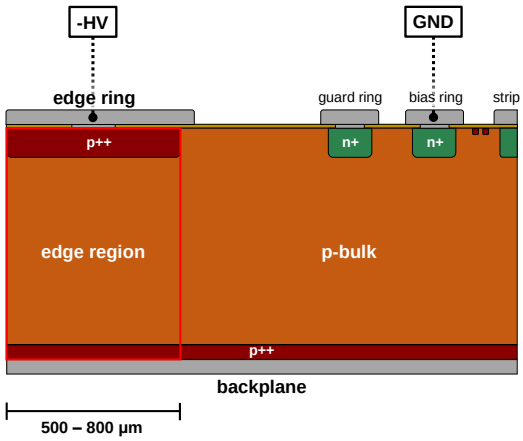

Figure 2: 2D sketch of an n-in-p strip sensor. It demonstrates the terminology used in this document and highlights the front-side biasing scheme. The bias ring is grounded while -HV is applied to the edge ring instead of the backplane (as it is the case for back-side biasing). Highly p-doped implants are located beneath the edge ring and on the bottom of the sensor bulk. Strip as well as guard and bias ring implants are n-doped. The red box highlights the region which we define as the edge.

3. Characteristic Measurements on Unirradiated Sensors

The edge needs to be protected from high electric fields, which is realized by a heavily doped edge implantation on the top-side. The implantation in combination with the broad aluminum layer right above is called the edge ring. It has several openings in the protective passivation layer for electrical contacting. The entire section below this aluminum ring is defined as the edge. The respective sensor regions are visualized and named in Figure 2. The edge dimensions in addition to the material related resistivity, ρ, fully determine the edge resistance, R_{edge}. The definition of the edge area, A_{edge}, is an important aspect. Our definition of the edge region is shown in Figure 2. It is given by the sensor layout and can be calculated by adding up the area between cutting edge and inner border of the edge implant. This definition is based on simulations presented in Chapter 5. Even at low bias voltages the depletion zone extends as far as the region beneath the edge ring (Figure 7).

As an initial simple check on how the biasing schemes of front-side biasing and back-side biasing might differ one can measure the current-voltage (IV) and capacitance-voltage (CV) characteristics. For FSB the HV was applied as depicted in Figure 2. Respective plots are shown in Figure 3 and 4 for two different samples of differing size. As shown in Table 1, C240 is larger than B240, which results in higher leakage current and capacitance at a given bias voltage. However, it is not possible to observe any difference between the FSB and BSB schemes. From this result one can conclude that the resistance of the sensor

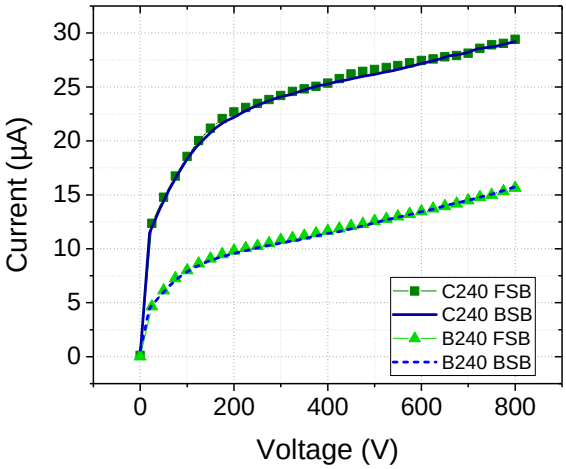

Figure 3: Comparison of front-side-biased and back-side-biased IV measurements performed on two mini sensors of differing size.

edge in this state must be very small, which results in a negligible voltage drop, ΔV, across the sensor edge. The effective bias voltage applied between the bulk and bias ring, V_{eff}, is therefore of the same value as the applied bias voltage, V_{bias}. These quantities relate as follows:

$$V_{\text{eff}} = V_{\text{bias}} - \Delta V \ . \tag{1}$$

4. Impact of Edge Dimensions

Edge resistivity measurements before irradiation revealed that the IV characteristic of the edge follows Ohm's law. After extracting the measured resistance, one can use the resistor formula to calculate the resistivity, ρ, which is a material constant and independent of dimensions:

$$\rho = R_{\text{edge}} \cdot \frac{A_{\text{edge}}}{L} \ , \tag{2}$$

where A_{edge} is the edge area and R_{edge} is the edge resistance. The length L of this resistor is equal to the active thickness of the material. This is because the highly doped, deep-diffused backside layer has a negligible resistance, since ρ is inversely proportional to the effective doping concentration (N_{eff}) [12]:

$$\rho = \frac{1}{q\mu|N_{\text{eff}}|} \ , \tag{3}$$

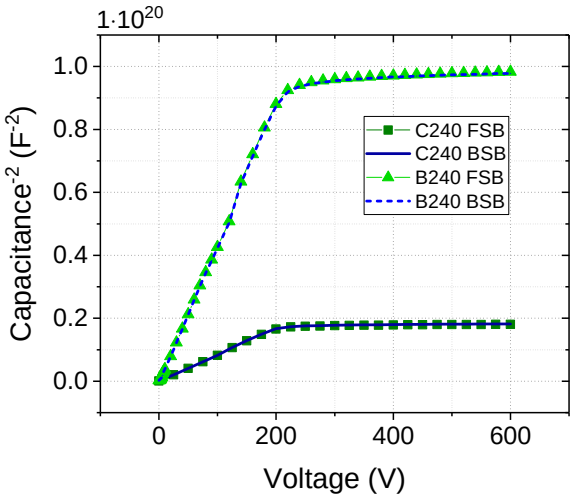

Figure 4: Comparison of front-side-biased and back-side-biased CV measurements performed on two mini sensors of differing size.

where q is the electron charge, μ is the carrier mobility of holes, and N_{eff} is the effective doping concentration, which is defined by the difference between acceptor and donor concentration. With a doping concentration of about $1 \cdot 10^{19}\,\text{cm}^{-3}$ the resistivity of the backside layer is below $1\,\Omega$cm and therefore several orders of magnitude smaller than the bulk resistivity [13].

The linear IV characteristics illustrated in Figure 5 indicate the validity of the assumptions made above. Voltage ramps were performed in steps of millivolts up to 1 V at room temperature. Depending on the size of A_{edge} and the bulk resistivity of the sample, a few millivolts suffice to induce currents of several 100 µA. The resistance is calculated by using the inverse slope of these curves. Since B240 and C240 are of the same material and thickness, the differing resistances can only stem from different edge dimensions (Table 1). The comparison of two ddFZ sensors with different active thickness (B200 and B240) shows that the resistance of the 200 µm material is lower, although the physical thickness is the same. This result supports the assumption that only the active thickness contributes to ρ. However, the difference in resistance is rather small and might seem close to the expected uncertainties, which weakens the argument. On the other hand, the difference is expected to be small. The ratios of active thickness and edge resistance are comparable:

$$\frac{L_{\text{B200}}}{L_{\text{B240}}} = 0.83 \approx \frac{R_{\text{B200}}}{R_{\text{B240}}} = 0.88\ . \tag{4}$$

To additionally validate this assumption, the resistance of the edge region was simulated in TCAD with a typical bulk resistivity for HPK material of $3\,\text{k}\Omega$cm.

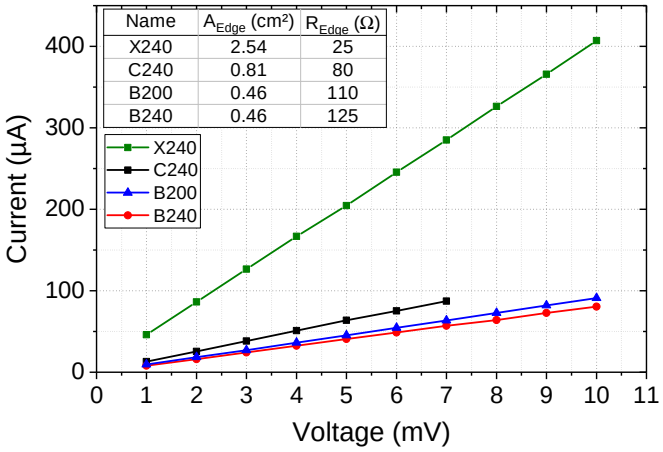

Figure 5: Illustration of four edge resistivity measurements.

An active thickness of 200 µm results in a resistance of 113 Ω, while a thickness of 240 µm yields a resistance of 137 Ω. These simulations confirm the previous statement.

As a next step, one can compare the resistivity obtained by edge resistivity measurements, ρ_{ER}, with the resistivity ρ_{CV}, which is taken from CV measurements on diodes of the respective material [12]:

$$\rho = \frac{L^2}{2\mu\epsilon_0\epsilon_{\mathrm{r}}V_{\mathrm{fd}}} \ , \tag{5}$$

where L is the active thickness, ϵ_0 is the electric field constant, ϵ_{r} is the relative permittivity of silicon, and V_{fd} the full depletion voltage[2]. A summary of those results is given in Table 3. The values are comparable. The highest deviation is observed for 200 µm ddFZ material.

While the fitting error ΔR is negligible, the deviation of the active thickness ΔL is given by the manufacturer and is about 5% (~ 10 µm). This represents the largest contribution to the uncertainties on ρ_{CV}. In addition, the deviation between ρ_{ER} and ρ_{CV} is higher for HPK than for IFX material. It is 10% for 240 µm and 21% for 200 µm ddFZ samples, whereas thinned IFX samples show a deviation of only 3% (Table 3). This is most likely a consequence of the deep diffused processing. The doping profile, and more importantly the transition region, becomes flatter with thicker backside implantation. Hence, V_{fd} and

[2]The capacitance increases with voltage and saturates as soon as the bulk is fully depleted. The knee of the CV curve determines the full depletion voltage.

Table 3: Mean resistivities for different materials resulting from CV measurements on diodes [8] and edge resistivity measurements.

Material	ρ_{ER} (kΩcm)	ρ_{CV} (kΩcm)	$\rho_{\mathrm{ER}}/\rho_{\mathrm{CV}}$
240 μm, ddFZ (HPK)	2.7 $\pm$ 0.2	3.0 $\pm$ 0.1	0.90 $\pm$ 0.15
200 μm, ddFZ (HPK)	2.6 $\pm$ 0.4	3.3 $\pm$ 0.1	0.79 $\pm$ 0.10
200 μm, FZ (IFX)	6.3 $\pm$ 0.6	6.5 $\pm$ 0.3	0.97 $\pm$ 0.05

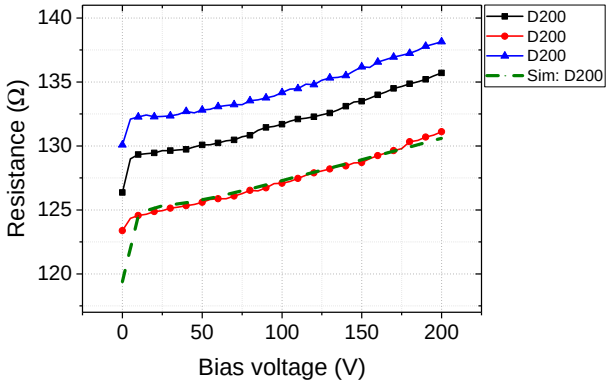

Figure 6: Resistance over bias voltage for IFX sensors. The markers represent experimentally found values on three different sensors of the same type, while full lines are drawn to guide the eye. Simulated results are depicted as a dashed line. The plot indicates that R_{edge} grows with increasing bias voltage.

the active thickness, L, become less well-defined. Moreover, the resistivities of those materials should be similar, but cannot expected to be equal, because of the different diffusion profiles. This has to be taken into account when comparing 240 µm and 200 µm ddFZ samples. In conclusion, the edge resistivity measurement is a valid and reliable method to estimate the resistivity of the edge region.

5. Bias Voltage Dependency

One can perform edge resistivity measurements and examine the impact of bulk depletion when using the biasing approach described in Chapter 2. The edge resistance is obtained by applying LV ramps to the edge and measuring the induced current. The bias voltage is applied to the bias ring by a second SMU to deplete the bulk. The results are shown in Figure 6. The dashed line represents a simulation of an IFX sensor with a charge density N_{ox} of $2 \cdot 10^{10}\,\mathrm{cm}^{-2}$ at the Si-SiO_2 interface. The solid lines represent measurements up to a bias voltage of 200 V. The simulation parameters N_{ox} and ρ were tuned to the red-lined

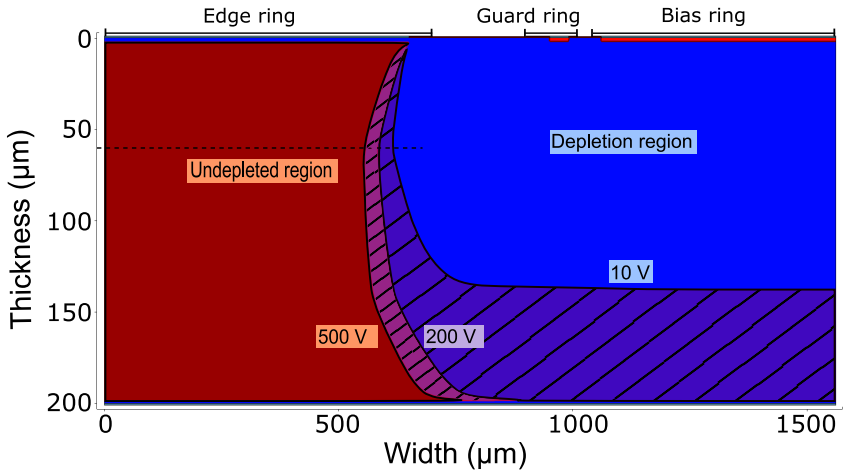

Figure 7: Simulation of the depletion volume for different bias voltages, namely 10 V (blue), 200 V (violet, lines with full spacing), and 500 V (magenta, lines with half spacing). The red region is the undepleted region. With increasing bias voltage the undepleted region underneath the edge ring becomes smaller.

D200 sensor. The simulated and the experimental results coincide and indicate a proportionality between R_{edge} and V_{bias}:

$$R_{\text{edge}} \sim V_{\text{bias}} \ . \tag{6}$$

The resistances of the measured IFX samples vary within 10 %. Thickness variations as discussed in the previous chapter as well as temperature variations (Chapter 6) are responsible for this. Moreover, defects at the edge due to dicing may provide additional ohmic paths.

The relation given by Equation (6) is a result of a phenomenon that we call Space Charge Region Constriction (SCRC). It can be explained best by visualizing the spread of the space charge distribution. Figure 7 shows the extent of these distributions for bias voltages of 10 V, 200 V, and 500 V. They extend from the bias ring towards backplane and edge ring. The dimension of the undepleted region beneath the edge ring is dependent on the width of the depletion region. It is clearly visible that the constriction of the edge region progresses as the bias voltage increases. As indicated by the black dashed line, the constriction turns out to be most prominent at $L = 60\,\mu\text{m}$ (distance from the top-side). The SCRC translates into an effective reduction of the edge width and therefore A_{edge}. Since ρ is inversely proportional to A_{edge} (Equation (2)), this results in an increasing resistance. Taking this into account, the SCRC approach models the relative increase of the resistance using the constriction length as a function of the bias voltage.

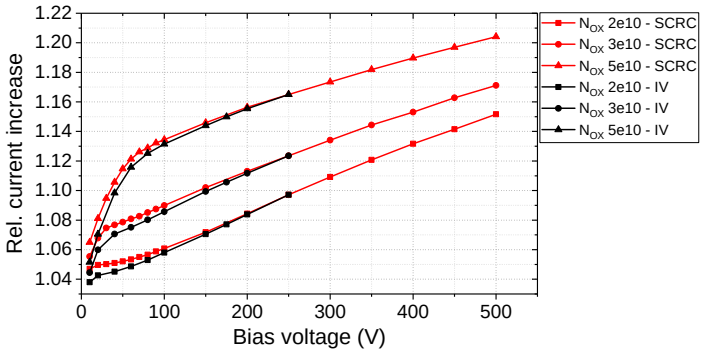

Figure 8: Relative increase of the current as a function of the bias voltage for different values of N_{ox}. The plot summarizes and compares the results of two methods that were used to simulate the impact of V_{bias} on R_{edge}. Red lines represent the outcome of the space charge region constriction method (SCRC). Black lines represent the characteristic gained by simulating the current through the edge and using Ohm's law.

For verification, the results of the SCRC simulation can be compared to the second, more straight forward method that was already applied in Figure 6: simulating an edge resistivity measurement to obtain the current through the edge, I_{edge}, for different voltages and calculating R_{edge}. The comparison of both methods is shown in Figure 8. It illustrates the relative current increase (normalized to a bias voltage of 250 V) as a function of the bias voltage for different N_{ox}. For voltages smaller than 10 V the SCRC approach cannot be used to deduce the resistance, because the depletion region does not extend into the edge region. The offset between the two methods at lower voltages in Figure 8 corresponds to a width variation of the SCRC of less than 10 µm, which is also the mesh size used for the simulation. This is negligible compared to the total edge width of 650 µm. To conclude, both methods produce qualitatively similar results that resemble the experimental findings.

6. Temperature dependence before irradiation

As presented in Figure 9, edge resistivity measurements between −20 °C and +20 °C indicate that ρ is proportional to temperature:

$$\rho \sim T \ . \tag{7}$$

A temperature difference of 40 °C results in a resistance growth of 36 %. This temperature dependence is in agreement with theoretical evaluations as explained below.

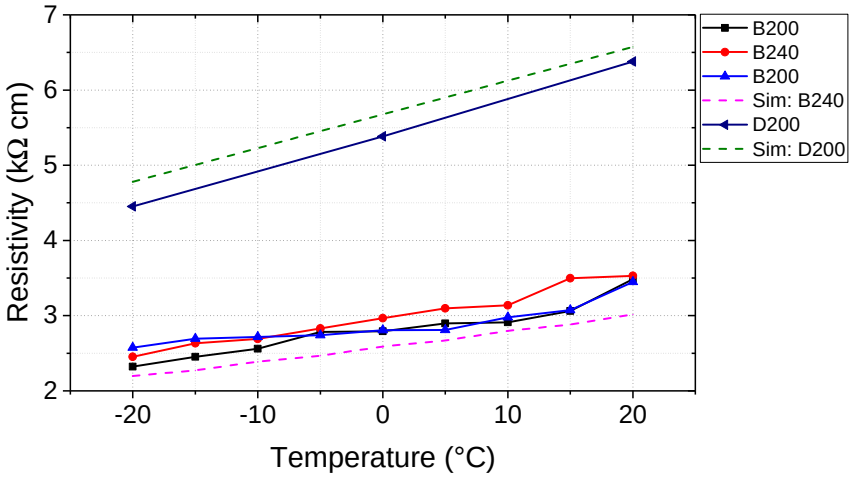

Figure 9: Edge resistivity measurements as a function of temperature between −20 °C and +20 °C. A bias voltage of 0 V was chosen because the impact of V_{bias} has already been discussed in the former chapter. The measurements indicate the expected characteristics described in Equations (7) and (8).

The resistivity ρ, which is the inverse of the conductivity σ, can be expressed as a function of the electron charge q, the carrier densities p and n as well as the carrier mobilities μ_{h} and μ_{e}:

$$\rho = \frac{1}{\sigma} = \frac{1}{q(n\mu_{\mathrm{e}} + p\mu_{\mathrm{h}})} \ . \tag{8}$$

Both carrier mobility and density are functions of temperature. Dopants are completely ionized in a temperature range between roughly −170 °C and 130 °C (100 K and 300 K). Hence, the carrier density is determined by the doping concentration and is therefore constant. This is referred to as the extrinsic or saturation region [13, 14, 15]. Since this is the temperature region in which all measurements were performed, the carrier mobility becomes the determining factor. The total carrier mobility, μ_{t}, is a superposition of two processes. As stated by Matthiessen's law, these two contributions are related to phonons and impurities:

$$\frac{1}{\mu_{\mathrm{t}}} = \frac{1}{\mu_{\mathrm{imp}}} + \frac{1}{\mu_{\mathrm{pho}}} \ . \tag{9}$$

At low temperatures the carrier mobility is dominated by the μ_{imp}-term. The process is determined by increasing ionization and impurity scattering. With increasing temperature phonon scattering begins to dominate, which leads to an inverted temperature dependence [13, 14]:

Table 4: Fit parameters regarding Equation (12) and the data presented in Figure 9.

Sensor name	R_0 ($\mathrm{k\Omega\,cm}$)	R_1 ($\mathrm{k\Omega\,cm\,K^{-\frac{3}{2}}}$)
B200	-1631 ± 498	0.98 ± 0.11
B240	-1912 ± 302	1.08 ± 0.07
B200	-312 ± 549	0.71 ± 0.12
B240 Simulation	-1142 ± 62	0.83 ± 0.01
D200	-3379 ± 76	1.94 ± 0.02
D200 Simulation	-2511 ± 87	1.81 ± 0.02

$$\frac{1}{\mu_{\mathrm{imp}}} \sim T^{-3/2} \,, \tag{10}$$

$$\frac{1}{\mu_{\mathrm{pho}}} \sim T^{3/2} \,. \tag{11}$$

According to Equation (8), the resistivity must therefore increase with temperature and is approximately proportional to $T^{\frac{3}{2}}$. Fits were made following this characteristic to be able to numerically evaluate the temperature dependence of the resistivity:

$$R = R_0 + R_1 \cdot T^{\frac{3}{2}} \,. \tag{12}$$

The temperature values were converted from °C to K. The fit parameters are listed in Table 4 for each sample. The comparability of the fit results supports the theoretical assumptions. The fact that the shape of the plotted curves in Figure 9 does not resemble the characteristic of a $T^{\frac{3}{2}}$-function (they appear to be rather linear) is a consequence of the relatively small temperature range. In conclusion, the presented experimental results are in agreement with theoretical evaluations.

7. Impact of Irradiation

As mentioned in Chapter 3, one can observe no significant difference between FSB and BSB measurements before irradiation. However, the situation changes after irradiation. Figure 10 shows the results of a front-side-biased and back-side-biased IV measurement of the same sensor, meaning that material properties and measurement parameters are identical. One can clearly observe a difference between FSB and BSB. Moreover, this characteristic turns out to be reversible. Changing the biasing scheme always yields the same result. The difference can therefore only originate from a lowered effective bias voltage V_{eff} as a consequence of a non-negligible voltage drop ΔV. The value of ΔV can be

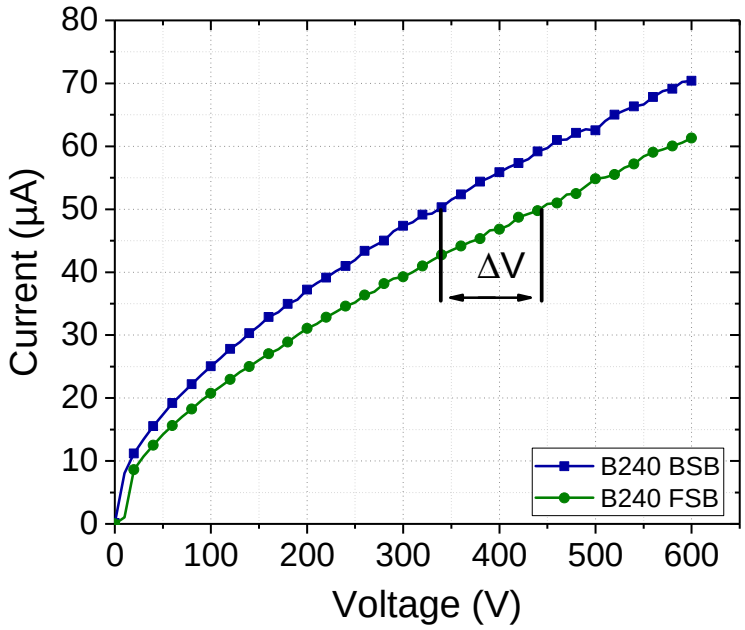

Figure 10: Leakage current comparison of an irradiated sensor irradiated with a fluence of $1 \cdot 10^{15}\,\mathrm{n_{eq}cm^{-2}}$ and operated via FSB and BSB at $-20°\mathrm{C}$. The difference between the curves is clearly observable at this fluence and is a result of a high R_{edge} after irradiation.

calculated from the shift of those two curves at a fixed leakage current value. At 50 µA this is about 100 V. On the other hand, if R_{edge} is known from edge resistivity measurements, one can calculate ΔV by using R_{edge} and the sensor's leakage current I:

$$\Delta V = R_{\mathrm{edge}} \cdot I \ , \tag{13}$$

where both R_{edge} and I are proportional to fluence. Hence, an irradiated front-side-biased sensor needs to be operated at higher bias voltages to compensate for ΔV. Otherwise the reduced V_{eff} yields lower charge collection efficiencies as compared to BSB, due to lower internal electric fields and reduced depletion. Since ΔV depends on the edge resistance of a sensor, this can only lead to the conclusion that the resistivity is significantly increased after irradiation. This statement is supported by edge resistivity measurements of irradiated sensors, which are shown in Figure 11. The edge resistivity, ρ, is increased by up to several orders of magnitude depending on the fluence.

The results of this study indicate that the increasing resistivity after irradiation must be driven by radiation induced defects in the silicon lattice and the

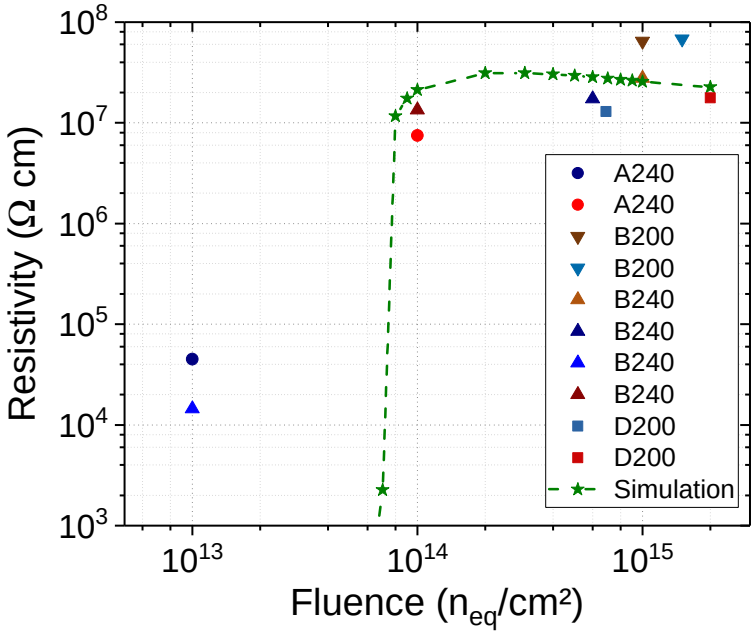

Figure 11: Extracted resistivity ρ from edge resistivity measurements on irradiated mini sensors for different fluences at a temperature of $-20°$C. The edge resistivity of the measured samples before irradiation was between 3 and 6 kΩcm. It increases by several orders of magnitude and starts to saturate at a fluence of $1 \cdot 10^{14}\,\mathrm{n_{eq}cm^{-2}}$.

respective changes of physical properties. These defects create additional states within the band gap, which are able to trap charge carriers for a certain amount of time. Due to the high amount of charge carriers injected from the contacts a certain fraction of traps are constantly occupied. This eventually results in a formation of a space charge region (SCR) within the edge. The emerging inner electric field opposes the current flowing through the edge, which eventually translates into an increased resistivity. This characteristic is also known as Space Charge Limited Current (SCLC). SCLCs in irradiated silicon samples have been evaluated in studies like the one reported in Ref. [16].

Although the increase of ρ is trap-induced and proportional to fluence, it does not increase linearly throughout the fluence spectrum. Looking at Figure 11, one can see that the resistivity seems to saturate between 10^7 and $10^8\,\Omega\,\mathrm{cm}$. A similar phenomenon was already described in Ref. [17]. Measurements reported in this reference, conducted at room temperature and after neutron irradiation, showed that the resistivity of different silicon samples saturated at a value between 200 and $300\,\mathrm{k}\Omega\,\mathrm{cm}$ close to the intrinsic resistivity. Moreover, the resistivity saturation is well correlated with the Fermi level stabilisation near the

mid-gap position as observed and described in Ref. [18].

The simulation in Figure 11 is done with the radiation model parameters listed in Table 2. A simplified geometry is used, where two highly doped p-type implants sandwich a p-type silicon bulk. This configuration corresponds to the edge region. The radiation model is known to work only in a fluence region between $1 \cdot 10^{14}\,\mathrm{n_{eq}cm^{-2}}$ and $1 \cdot 10^{15}\,\mathrm{n_{eq}cm^{-2}}$. Therefore, simulated data below $1 \cdot 10^{14}\,\mathrm{n_{eq}cm^{-2}}$ are not expected to reproduce experimental results. Nevertheless, a saturation of the resistivity is indicated within the model range of validity.

Furthermore, the data shown in Figure 12 reveal that ρ is not increasing with temperature in a range of $-20\,^{\circ}\mathrm{C}$ to $+20\,^{\circ}\mathrm{C}$ after irradiation. The dependency is inverted and described best by an exponentially decreasing function:

$$\rho = \rho_0 \cdot \mathrm{e}^{-\beta \cdot T} \ . \tag{14}$$

The temperature is converted from °C to K for this fit. Its parameters are summarized in Table 5.

Figure 12 summarizes the results obtained from several edge resistivity measurements. The measurements were performed with $V_{\mathrm{bias}} = 0\,\mathrm{V}$, because the impact of bias voltage after irradiation is negligible. A measurement of B200 at $V_{\mathrm{bias}} = 600\,\mathrm{V}$ was added to the plot to prove that point. The data show that a temperature variation of $40\,^{\circ}\mathrm{C}$ leads to a resistance change of almost $600\,\%$ for A200 ($\Phi = 1 \cdot 10^{13}\,\mathrm{n_{eq}cm^{-2}}$). For B200 ($\Phi = 1 \cdot 10^{15}\,\mathrm{n_{eq}cm^{-2}}$) it is beyond $6600\,\%$. The scattering mechanisms of intrinsic silicon that define the temperature dependence before irradiation are completely superposed by trap-dominated processes. Like the sensor leakage current, these processes tend to be very temperature dependent, as shown by the high resistivity change after irradiation. Studies about temperature dependence of trapping-processes as in Ref. [19] have shown that the trapping lifetime, τ, as well as the trapping probability, $P(\tau)$, are inversely proportional to temperature. Thus, the probability of charge carriers getting trapped decreases the higher the temperature. This results in lower space charge concentration and lower opposing electric field, therefore faster drift, higher current, and finally a lower edge resistance.

8. Annealing effects

This chapter discusses the impact of annealing on the edge resistivity. For this purpose, measurements of ρ were performed on a D200 sensor irradiated to a fluence of $6.82 \cdot 10^{14}\,\mathrm{n_{eq}cm^{-2}}$. In particular, ρ was measured at different bias voltages and for different annealing times. The temperature during the measurement was $-20\,^{\circ}\mathrm{C} \pm 0.3\,^{\circ}\mathrm{C}$. Annealing steps ranging from 0 minutes to 50 minutes at 60°C were performed. Therefore the sensor was in the region of beneficial annealing at all times. The results are shown in Figure 13. It is clearly

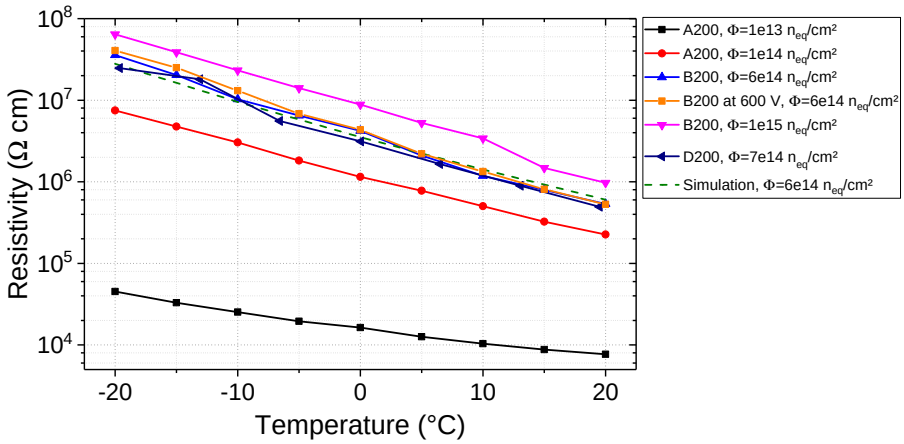

Figure 12: Edge resistivity measurements of irradiated sensors for temperatures between $-20\,^{\circ}\mathrm{C}$ and $+20\,^{\circ}\mathrm{C}$ at $V_{\mathrm{bias}} = 0\,\mathrm{V}$. A measurement at $V_{\mathrm{bias}} = 600\,\mathrm{V}$ was added to confirm the negligible impact of the bias voltage after irradiation. The plot indicates that ρ is inversely proportional to temperature.

Table 5: Summary of fit parameters regarding Equation (14) and the data presented in Figure 12 for $V_{\mathrm{bias}} = 0$.

Φ ($\mathrm{n_{eq}cm^{-2}}$)	Sensor name	ρ_0 ($\mathrm{k\Omega\,cm}$)	β ($\frac{1}{K}$)
$1 \cdot 10^{13}$	A200	10	0.067 ± 0.003
$1 \cdot 10^{14}$	A200	1162 ± 36	0.093 ± 0.001
$6 \cdot 10^{14}$	B200	3267 ± 275	0.119 ± 0.004
$1 \cdot 10^{15}$	B200	8556 ± 205	0.101 ± 0.001

observable that the resistivity increases with increasing annealing times, which is most prominent within the first 5 minutes. At 1000 V bias voltage the edge resistivity for the unannealed sensor was about $20\,\mathrm{M\Omega\,cm}$. After 50 minutes of annealing the resistivity increased to about $25\,\mathrm{M\Omega\,cm}$.

During beneficial annealing the acceptor concentration and therefore $|N_{\mathrm{eff}}|$ decreases as shown in Ref. [20]. The observed increase of resistivity with annealing time as a consequence of decreasing $|N_{\mathrm{eff}}|$ is described by Equation (3). It should be noted that the defects responsible for donor and acceptor generation, which change with annealing, are not on the same energy level within the band gap as the ones responsible for trapping [20, 21]. Therefore, the observations presented in Figure 13 are different from the ones discussed in Chapter 7. Actually, traps do not necessarily undergo annealing. If this was always the case, it would lead to a change in resistivity in the opposite direction. Another confirmation of

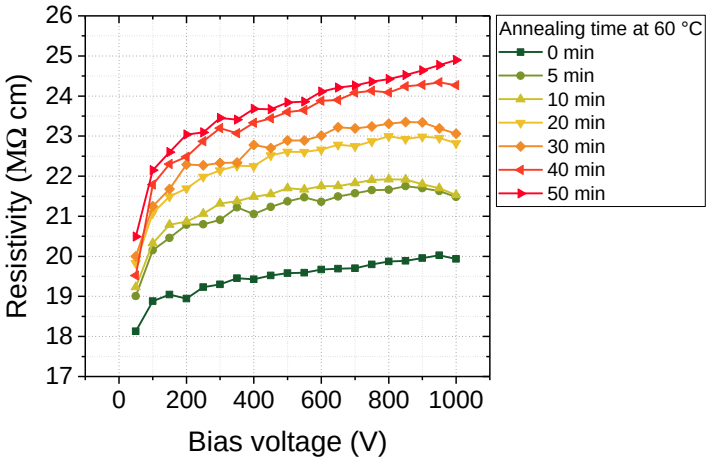

Figure 13: Measured resistivity of a D200 sensor irradiated to a fluence of $6.82 \cdot 10^{14}\,\mathrm{n_{eq}cm^{-2}}$ with 23 MeV protons, as a function of the bias voltage and different annealing times.

the decrease of N_{eff} during beneficial annealing is given in Ref. [22]. It presents annealing studies of p-type diodes, which were irradiated with 24 GeV protons. Since our measurements only include proton irradiated samples, it should be mentioned that neutrons have a different impact on N_{eff} than protons. Moreover, the annealing of neutron generated defects differs from the ones generated by protons. However, the conclusion of the given references is that $|N_{\mathrm{eff}}|$ always decreases during beneficial annealing and increases during reverse annealing, independent of the radiation particle type.

Figure 14 shows a TCAD simulation of the edge resistivity for different acceptor and donor trap concentrations (defects that undergo annealing). The acceptor (or donor) trap concentration in the TCAD model is the defect concentration, which effectively behaves like the acceptor (or donor) concentration. More acceptor traps in the TCAD model mean effectively more acceptors in the bulk. A simplified structure of 200 µm thick p-type bulk with a high p-type implantation on both sides for the two contacts is used to simulate the edge ring. Voltage ramps from 0 V to 1 V are performed on one contact and the current is measured on the other. Using the inverse slope of the IV curve the resistance and resistivity can be calculated. To approximately model the effects of annealing, the acceptor and donor trap concentrations $N_{\mathrm{A},\Phi}$ and $N_{\mathrm{D},\Phi}$ for a fluence of $6.82 \cdot 10^{14}\,\mathrm{n_{eq}cm^{-2}}$ are varied. Along the black dotted line in Figure 14 one can see the change in edge resistivity for different $N_{\mathrm{A},\Phi}$. The simulation confirms the previous statement that decreasing acceptor concentration leads to an increase in edge resistivity. The radiation model parameters used are listed in Table 2. It should be noted that a more detailed modelling of the annealing behaviour is far more complex. Changes in the donor trap concentration

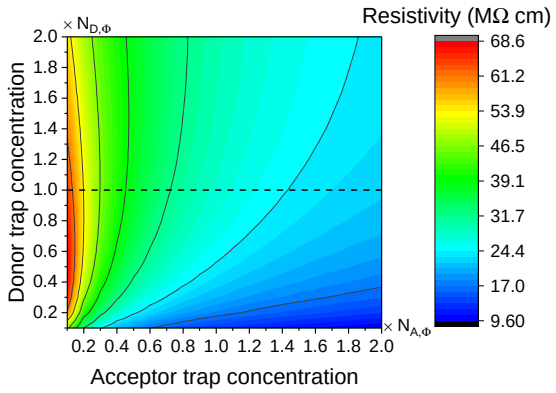

Figure 14: Simulation of the edge resistivity for varying acceptor and donor trap concentrations. $N_{A,\Phi}$ and $N_{D,\Phi}$ represent the acceptor and donor trap concentrations at a fluence of $6.82 \cdot 10^{14}\,n_{eq}cm^{-2}$ according to the irradiation model used in this work. Decreasing the acceptor trap concentration and hence the effective acceptor concentration increases the resistivity, as is expected from beneficial annealing.

and the electron and hole capture cross sections need to be considered as well [9].

For reverse annealing we would expect the opposite behaviour. It has been shown in Ref. [20] that reverse annealing increases the acceptor concentration. According to the results of this study, this would lead to a decrease of the edge resistivity. Typical measurements confirming this behaviour can be found in Ref. [23]. The test device used in that reference was a silicon test structure with an ohmic contact on top and one on the bottom. This is comparable to the configuration at the edge region. The unirradiated bulk resistivity was between 4 kΩcm and 6 kΩcm, which is similar to the IFX or HPK sensors. After neutron irradiation of $1.5 \cdot 10^{14}\,n_{eq}cm^{-2}$, the resistivity decreased after annealing from about 300 kΩ cm to about 200 kΩ cm when going from 38 hours of room temperature annealing (equals 17.18 minutes at 60°C) to 470 days of room temperature annealing (equals 5099.34 minutes at 60°C). The resistivity measurements were performed at room temperature. To check the validity of the resistivities in this chapter one may compare them with Figure 12. The sensors have comparable resistivity in the respective measurements at -20°C and at room temperature.

9. Extrapolation to Large Sensors

Based on the results presented in previous chapters, one can approximate the voltage drop of a large, irradiated sensor by taking into account the measured edge resistivity of a mini sensor. The desired maximal operation voltage of a typical HEP tracking device such as the Phase-2 Outer Tracker of CMS is 600 V. The expected operation temperature of a sensor is about −20 °C. The expected fluence for the detector modules is simulated to be between $3 \cdot 10^{14}\,n_{eq}cm^{-2}$

and $1 \cdot 10^{15}\,\mathrm{n_{eq}cm^{-2}}$ for an integrated luminosity of $3000\,\mathrm{fb^{-1}}$. A fluence of $6 \cdot 10^{14}\,\mathrm{n_{eq}cm^{-2}}$ seems appropriate for this example, since it is roughly the median of those values and was covered by our measurements. The leakage current at this voltage, fluence, and temperature can be approximated by using the damage rate α [20] after an annealing of 80 minutes at 60°C for a typical sensor of 10 cm x 10 cm x 240 µm like X240. This yields roughly 1 mA. The edge resistivity of a similarly irradiated mini sensor (B240, $\Phi = 6 \cdot 10^{14}\,\mathrm{n_{eq}cm^{-2}}$) is about $17.3\,\mathrm{M\Omega\,cm}$. One can assume that ρ is a material constant and therefore equal for B240 and X240. Considering the dimensions of X240, one finds the edge resistivity to be about $166\,\mathrm{k\Omega}$. Since leakage current equates to the current that flows through the edge of a front-side-biased sensor, one can calculate ΔV by using Equation (13). According to these assumptions and given parameters, the voltage drop would be 158 V. Multiplying this value with the expected leakage current yields an additional power consumption of 0.15 W per sensor. The CMS Outer Tracker for example consists of roughly 26 000 strip sensors. The additional power consumption would then total 3900 W. More importantly, the additional bias voltage that is necessary to deplete the sensor would exceed the high voltage robustness of the module design [11]. However, reducing the fluence in this calculation to $1 \cdot 10^{13}\,\mathrm{n_{eq}cm^{-2}}$ would result in a voltage drop of less than 1 V and a negligible additional power consumption. Such a magnitude would correspond to the expected fluence in the LHCb experiment [24].

10. Conclusions

Module assembly for large silicon trackers could benefit from FSB due to single-sided procedures. The sensor back-side can be connected via the conductive edge from the top-side. The validity of this biasing scheme was studied with respect to temperature and radiation on n-in-p sensors. Measurements were performed independently at ETP and HEPHY with different materials. The results are in agreement. The data were interpreted and complemented by simulations. FSB is accompanied by a voltage drop along the sensor edge, which is determined by the edge resistance of a sensor. High radiation levels in addition to low temperatures increase the edge resistance by several orders of magnitude. For large sensors, this results in a high voltage drop and additional power consumption in order to reach the desired effective bias voltage. The increased bias voltage requires modifications of the module design in order to increase the high voltage robustness. In the case of the Phase-2 Outer Tracker of CMS with sensors of about 10 cm x 10 cm and expected fluences between $3 \cdot 10^{14}\,\mathrm{n_{eq}cm^{-2}}$ and $1 \cdot 10^{15}\,\mathrm{n_{eq}cm^{-2}}$, these disadvantages cannot be outweighed by the benefits of FSB and therefore disqualify FSB as a biasing concept. However, there are HEP experiments with lower expected fluences that could benefit from FSB. The disadvantages could also be minimized by reducing the sensor dimensions, the thickness and the resistivity of the material, as well as increasing the edge area or increasing the operation temperature.

11. Acknowledgements

The sensors were developed and produced in the framework of the CMS Phase-2 Tracker Upgrade activities. The collaboration kindly agreed to let us use the sensors for this study.

The research leading to these results has been co-funded by the European Commission under the Horizon 2020 Research Infrastructures project AIDA-2020, Grant Agreement 654168.

The research leading to these results has received funds from the call "Forschungspartnerschaften" of the Austrian Research Promotion Agency (FFG) under the grant no. 849087.

References

[1] Hamamatsu Photonics K.K., Japan. http://www.hamamatsu.com.

[2] Infineon Technologies Austria AG. https://www.infineon.com.

[3] T. Bergauer, "Silicon sensor prototypes for the Phase II upgrade of the CMS tracker", *Nucl. Instr. and Meth.* **831** (2016) 161–166.

[4] Institut für Experimentelle Teilchenphysik, Germany. https://www.etp.kit.edu/.

[5] Karlsruher Institut für Technologie, Germany. https://www.kit.edu/.

[6] Institut für Hochenergiephysik, Austria. http://www.hephy.at/.

[7] Synopsys Inc., USA. https://www.synopsys.com/silicon/tcad.html.

[8] T. Bergauer et al., "First thin AC-coupled silicon strip sensors on 8-inch wafers", *Nucl. Instrum. and Meth.* **830** (2016) 473–479.

[9] R. Eber, "Untersuchung neuartiger Sensorkonzepte und Entwicklung eines effektiven Modells der Strahlenschädigung für die Simulation hochbestrahlter Silizium-Teilchendetektoren". PhD thesis, Karlsruher Institut für Technologie (KIT), 2013.

[10] Zyklotron AG, Germany. http://www.zyklotron-ag.de.

[11] CMS Collaboration, "The Phase-2 Upgrade of the CMS Tracker", Technical Report CMS-TDR-014, CERN, Geneva, 2017.

[12] F. Hartmann, "Evolution of Silicon Sensor Technology in Particle Physics". Springer Tracts in Modern Physics. Springer Berlin Heidelberg, 2008.

[13] V. Zeghbroeck, "Principles of Semiconductor Devices and Heterojunctions". Prentice Hall PTR, 2007.

[14] M. Grundmann, "The Physics of Semiconductors: An Introduction Including Nanophysics and Applications". Springer Berlin Heidelberg, 2010.

[15] G. Lutz, "Semiconductor Radiation Detectors: Device Physics". Springer Berlin Heidelberg, 2007.

[16] A. Taroni and G. Zanarini, "Space charge limited currents in P-N junctions", *J. Phys. Chem. Solids* **30** (1969) 1861 – 1871.

[17] Z. Li, "Radiation damage effects in Si materials and detectors and rad-hard Si detectors for SLHC", *JINST* **4** (2009) P03011.

[18] V. Eremin and Z. Li, "Determination of the Fermi level position for neutron irradiated high resistivity silicon detectors and materials using the transient charge technique (TChT)", *IEEE Trans. Nuc. Sci.* **41** (1994) 1907–1912.

[19] G. Kramberger et al., "Effective trapping time of electrons and holes in different silicon materials irradiated with neutrons, protons and pions", *Nucl. Instr. and Meth.* **481** (2002) 297 – 305.

[20] M. Moll, "Radiation damage in silicon particle detectors: Microscopic defects and macroscopic properties". PhD thesis, Hamburg University, 1999.

[21] A. Junkes, "Influence of Radiation Induced Defect Clusters on Silicon Particle Detectors". PhD thesis, Hamburg University, 2011.

[22] H. Hoedlmoser, M. Moll, M. Koehler, and H. Nordlund, "CCE measurements and annealing studies on proton-irradiated p-type MCz silicon diodes", *Nucl. Instr. and Meth.* **583** (2007) 64 – 70.

[23] Z. Li, "Elevated temperature annealing behaviors of bulk resistivity and space charge density of neutron irradiated silicon detectors and materials", *Nucl. Instr. and Meth.* **368** (1996) 353 – 363.

[24] M. Siegler, F. Lehner, M. Needham, and O. Steinkamp, "Expected Particle Fluences and Performance of the LHCb Trigger Tracker", LHCb Note 2004-070 (2004).